Available online at www.sciencedirect.com

ScienceDirect

Advances in Space Research 70 (2022) 699–709

ADVANCES IN SPACE RESEARCH
(a COSPAR publication)

www.elsevier.com/locate/asr

All-sky imaging observations of mesospheric fronts from Silchar (24.7°N, 92.8°E)

Nilesh Chauhan [a], S. Gurubaran [a,*], S. Moulik [b], P.K. Das [b], Mala Bagiya [a]

[a] Indian Institute of Geomagnetism, New Panvel (W), Navi Mumbai 410 218, India
[b] Magnetic Observatory, Silchar 788 011, India

Received 4 December 2021; received in revised form 1 May 2022; accepted 7 May 2022
Available online 14 May 2022

Abstract

An All-Sky Airglow Imager was operated at Silchar (24.68°N, 92.76°E), India from 9 to 11 December 2018, during a special observational campaign. We report the presence of two simultaneous mesospheric fronts observed in OH airglow emission propagating orthogonal to each other on the night of 9 December 2018, which was a rare and unique observational feature. A third mesospheric front was observed on 11 December 2018. Temperature and OH intensity measurements from SABER instrument onboard TIMED satellite were used to characterise the environment of the frontal propagation. Though one of the frontal structures resembled a mesospheric bore, the other frontal events do not satisfy a few of the requirements to be met for a bore. We also report the modulation of the OH emission layer by the passage of the mesospheric front on the night of 11 December 2018.

Keywords: Gravity Waves; Mesospheric Fronts; Bores; Ripples; Airglow Imaging

1. Introduction

A mesospheric front is marked by an extensive step-like onset of enhanced or depleted airglow intensity, which divides the night sky into dark and bright regions followed by alternating crests and troughs of intensity (categorised as waves) or turbulence. Several frontal events have been reported earlier, and they are generally classified into two groups: (1) wall events (e.g., Batista et al., 2002; Li et al., 2007; Swenson and Espy, 1995) and (2) bore events (Bageston et al., 2011; Brown et al., 2004; Fechine et al., 2005, 2009; Fritts et al., 2020; Medeiros et al., 2005, 2016, ;Narayanan et al., 2009b, 2012, 2021 Pautet et al., 2018; She et al., 2004; Smith et al., 2003, 2005). Each group of these frontal events reflects distinctly different frontal wave phenomena, yet they all display similar characteristics in all-sky airglow images. Thus, a careful interpretation is required to distinguish them. The bore, for example, requires a duct or a channel to propagate. This can be a thermal (e.g., Meriwether et al., 1998; She et al., 2004; Smith et al., 2003) or a Doppler (e.g., Fechine et al., 2009) duct or a combination of both (e.g., Bageston et al., 2011; Narayanan et al., 2021). The ducts enable long-distance propagation of gravity waves, particularly when energy dissipation is neglected (e.g., Dewan and Picard, 2001). Thus, they provide an effective means of wave energy and momentum transport over large distances in the atmosphere.

In this work, we report three mesospheric frontal events observed by an all-sky airglow imager on the nights of 9 and 11 December 2018 over the low latitude Indian site, Silchar (24.7°N, 92.8°E). Out of the two nights, the observations on 9 December 2018 were peculiar in that we noticed a quasi-monochromatic gravity wave and a mesospheric front propagating antiparallel to each other, with

* Corresponding author.
E-mail address: gurubaran.s@iigm.res.in (S. Gurubaran).

https://doi.org/10.1016/j.asr.2022.05.011
0273-1177/

a simultaneous propagation of a second front orthogonal to both. Another front was observed on 11 December 2018 that propagated almost antiparallel to the direction of one of the fronts observed on 9 December 2018. Coincident temperature and OH 1.6 μm emission profiles obtained from the Sounding of the Atmosphere using Broadband Emission Radiometry (SABER) instrument on board the Thermosphere Ionosphere Mesosphere Energetics and Dynamics (TIMED) satellite (Russell et al., 1999) are utilized in this work to assess the environmental conditions that prevailed at the time of frontal propagation. Using the criteria given by Dewan and Picard (1998, 2001), and based on the prevailing understanding, the frontal event observed on 9 December 2018 was inferred to be a mesospheric bore. On the night of 11 December 2018, we report a severe modulation of the OH emission layer, and we ascribe this to the propagation of the mesospheric front occurring around this time.

2. Observations

The all-sky airglow imaging observations commenced at the Magnetic Observatory of Indian Institute of Geomagnetism within the Assam University campus at Silchar, India, during November 2017. The site is located at a distance of ~500 km from the Himalayas in the north and at a similar distance from the Bay of Bengal. The Himalayas can be the potential sources of orography generated gravity waves. The contribution of the Himalayan orography to the gravity wave generation (Liu et al., 2019; Miller et al., 2015; Ramkumar et al., 2021) is poorly understood, making this location a useful site for gravity wave studies. Moreover, the Bay of Bengal can be a source of convectively generated gravity waves (Bindu et al., 2016; Dutta et al., 2009; Niranjan Kumar and Ramkumar, 2008; Rakshit et al., 2018), especially during the monsoon season. Further, the southeast Asian maritime continent of Indonesia provides hotspots for atmospheric convective activity, which can be a source for gravity waves. Fig. 1 shows the location of the observing site along with the footprints of SABER passes on the nights of 9 and 11 December 2018 (discussed later).

2.1. Data and methodology

The Silchar all-sky airglow imager, originally built by Keo Scientific Ltd., Canada, is equipped with interference filters tuned to monitor the OI green line at 557.7 nm, the sodium yellow line with center wavelength at 589.3 nm with 2 nm bandwidth (D1 and D2 lines of sodium at 589.0 and 589.6 nm, respectively), and the OI red line at 630.0 nm. A broadband filter is used to capture the OH Meinel band emission in the wavelength range 715–930 nm, along with a notch at 865 nm and a narrowband filter at 572.3 nm to monitor the background sky. The imager uses a Mamiya medium-format f/4 achromatic fisheye lens with a field of view (FOV) of 180°. The CCD detector has an ultrafast Cannon lens (f/0.95), is back-illuminated and operates with 1024 × 1024 pixels at a pixel depth of 16 bits. The physical dimension of the CCD array is 13.3 mm × 13.3 mm with a pixel size of 13.3 μm. The camera system is thermoelectrically cooled to −70 °C during image acquisition. Observations were conducted in special campaigns during November-December 2017, March and December 2018. From January 2020, the imager was moved to a specially constructed hut and is being operated continuously on moonless and cloud-free nights since then.

The December 2018 campaign was conducted on four nights from 8 to 11 December 2018. As stated earlier, in this work we report three mesospheric frontal events and a quasi-monochromatic gravity wave observed on the nights of 9 and 11 December 2018. The observational details of these events are presented in the next section. It may be noted that along with airglow intensity variations across the sky that carry useful information about wave signatures, any light contamination from stars, city lights, etc. is also captured in all-sky images. To retrieve useful atmospheric wave parameters, several image processing steps are needed to be performed on the raw images. For this purpose, we adopt the procedure outlined in Garcia et al. (1997) and Narayanan et al. (2009a). As a first step, each of the pixels is tagged with a corresponding position in the sky using a star map. Bright stars are removed from the images using a median filter. An algorithm then identifies pixels with much higher intensity values than their surrounding 50 × 50 pixel area. When the difference between the intensities of the raw pixel and the median of the surrounding pixels exceeds a certain threshold value, the intensity of the raw pixel is replaced by the median value. We have applied subsequent time-differencing (TD) to individual images for easy visualisation, as this enables the contrast of smaller scale wave features to get enhanced. According to Swenson and Mende (1994), the time-differencing technique applied to all-sky images could introduce artefacts that would resemble a wave structure. Thus, care needs to be taken while drawing inferences from these TD images.

A set of TD images depicting the propagation of front in both these emissions obtained by this procedure is presented in Fig. 2. The dotted arrows in the top (557.7 nm images on 9 December 2018) and middle (OH images on 9 December 2018) panels indicate the front propagating towards southwest direction, while the dashed and solid arrows indicate the front observed in OH images on 9 December 2018 (propagating towards northwest direction) (middle panel) and 11 December 2018 (propagating towards southeast direction) (bottom panel), respectively. The solid arrow in the top panel shows the propagation direction (southeast) of a quasi-monochromatic gravity wave (QMGW) with its pronounced crests and troughs observed in 557.7 nm emission on 9 December 2018. We next project the TD images on to a geographic grid corresponding to the altitudes of airglow emission layers, namely, 87 and 97 km for OH and OI 557.7 nm emissions,

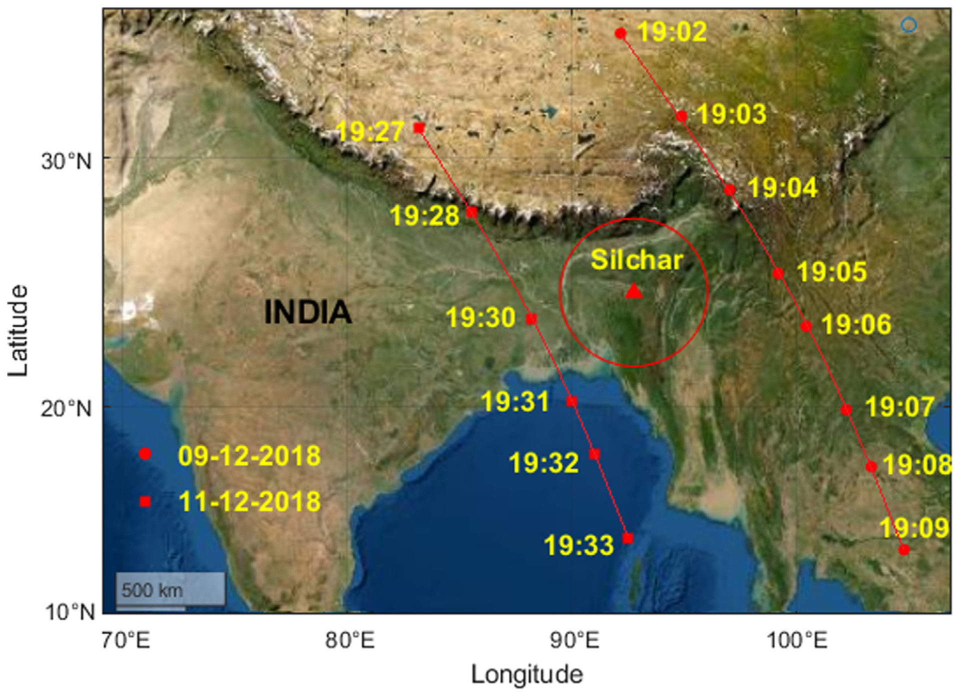

Fig. 1. Map showing the location of the observing site (solid triangle) along with the footprints of TIMED/SABER passes with the measurement times (in UT) on the nights of 9 and 11 December 2018 indicated. The great circle around the observation site represents the field of view of the all-sky imager corresponding to altitude of 97 km.

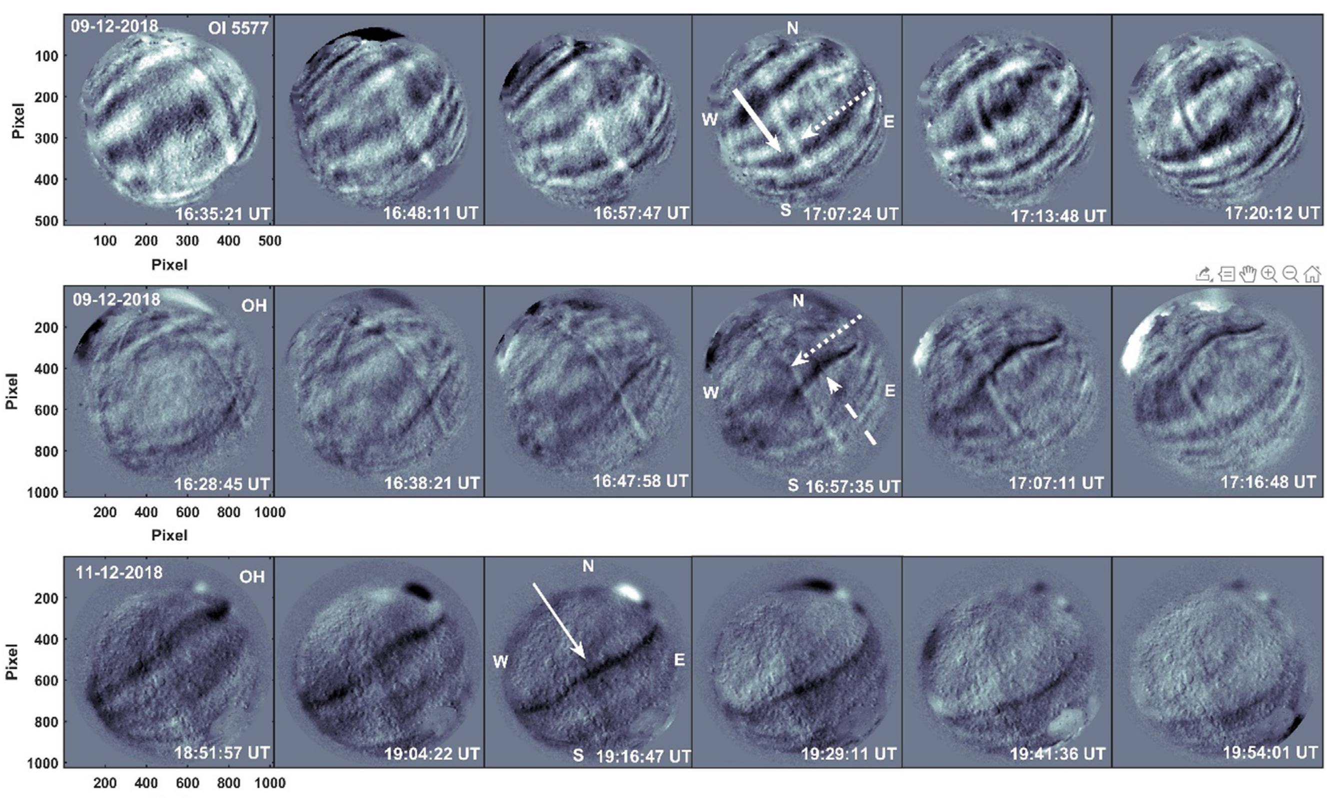

Fig. 2. Time-differenced images showing the frontal events observed on the nights of 9 December 2018 (top and middle panels) and 11 December 2018 (bottom panel). Details are presented in the text.

respectively. As a supplementary material to this article, we show a set of movies (M.1, M.2 and M.3) depicting the wave, ripple and the frontal structures observed on 9 and 11 December 2018.

Since no simultaneous ground-based mesospheric temperature measurements are available, we used the data sets on temperature and 1.6 μm OH volume emission rate (VER) for altitudes between 75 and 105 km obtained by the SABER instrument on board the TIMED satellite. In its limb viewing mode and while scanning the horizon, SABER measures atmospheric emissions in 10 broadband spectral channels ranging from 1.27 to 17 μm (Russell et al., 1999). Vertical profiles of kinetic temperature are retrieved from broadband measurements of CO_2 15 μm limb emission in the MLT region. On 9 December 2018, the SABER pass was available ~2 h after the event detected by the all-sky imager. Assuming that the horizontal extent of the observed mesospheric front was of the order of a few hundred to several hundreds of km, the SABER measurements at the locations shown in Fig. 1 are considered to represent the then background environment for the respective bore feature, more so, on 11 December 2018 when the SABER footprint appeared to overtake the bore front very close to the imager field of view.

Due to the non-availability of simultaneous wind measurements, we have utilised the updated Horizontal Wind Model (HWM-14) (Drob et al., 2015). This empirical model outputs comprising zonal and meridional winds for the specified range of location, altitude, and time are used in this work. As the model outputs need not represent the realistic wind scenarios, the calculations shown in Section 3 are to be treated with caution.

2.2. Observations on 9 December 2018

On 9 December 2018, the imaging observations commenced at 13:00 UT. At 15:53 UT, an intense, quasi-monochromatic gravity wave (QMGW) was recorded in OI 557.7 nm as well as in OH images, and subsequently this wave was seen propagating towards the southeast. This wave event was so intense in OI 557.7 nm emission that several crests and troughs could be identified in the images, as they propagated one after the other. The wave crests were more prominent in OI 557.7 nm images than in OH emission images. It can be seen in the sample images shown in Fig. 2 (top panel) that the wavefront covered almost an entire cross-section of the field of view, and thus the horizontal extent of the wavefront would have been at least ~500 km. The calculations performed over the entire sequence of images yielded an average horizontal wavelength of 46.3 ± 4 km and an average estimated phase speed of 90.7 ± 11 m/s, with the propagation of the QMGW directed towards an azimuth of 143° (from north (clockwise)). The wave event was observed until ~17:50 UT, after which the individual crests and troughs begin to break into smaller scale waves, as shown in Fig. 3. This would imply that the wave had attained saturation, was under the influence of instabilities, or would have gone through a critical level interaction.

Around the same time when the QMGW was observed, two mesospheric fronts were found to propagate in orthogonal directions and near simultaneously. In Fig. 4 we show a select set of TD images (OI 557.7 nm on the left panel and OH on the right panel), wherein one of the fronts (hereafter denoted by F1), indicated by dotted arrows, can be clearly seen.

The front F1 first appeared in the field of view of the imager at 16:12 UT in the north-east sky, and was visible in both OH and OI 557.7 nm images (marked by dotted arrows). The front appeared bright in OI 557.7 nm emission images, while it appeared dark in OH emission. With its alignment in the northwest-southeast direction, this frontal structure propagated towards the southwest at an azimuth of ~230°, which was in a direction orthogonal to the direction of propagation of the QMGW, though with a smaller average estimated phase speed of 35.6 ± 7 m/s. The front was followed by a gravity wave train, and this feature was similar to the previous observations of mesospheric undular bores (Bageston et al., 2011; Fechine et al., 2005, 2009; Medeiros et al., 2005; Narayanan et al., 2009b; She et al., 2004; Smith et al., 2003; Taylor et al., 1995). At least three wave crests were observed behind the front in both emissions. The average horizontal wavelength of the undulations was ~21 km. The front began to fade as it crossed the zenith and the undulations disintegrated into the background as shown in Fig. 5. This feature finally disappeared at 17:36 UT.

The observations reported here were similar to those of an earlier report by She et al. (2004). The front and its trailing waves along with the complementarity effect between OH and OI 557.7 nm images suggest that the front F1 could have been a mesospheric bore. Although the bright-and-dark complementarity between OH and OI 557.7 nm images observed herein was opposite to that predicted by Dewan and Picard (1998), it is noted from the literature that such a frontal feature can still be considered as a mesospheric bore, as the width and location of the duct responsible for this effect could be different in a real scenario from the predicted ones (Medeiros et al., 2005, for example). The ducting condition, which is necessary to form a bore, is discussed in Section 3.

During the period of frontal propagation, several ripple-like structures were also observed between 16:38 UT and 17:10 UT in OI 557.7 nm emission images (marked by rectangular boxes in Fig. 6). The phase fronts of these ripple structure were aligned parallel to the QMGW phase fronts, which suggest that they could have originated in dynamical instabilities acting on the QMGW. The wavelength of these ripples was found to be ~10 km, as they were propagating towards north-east, i.e., in the direction of their phase fronts. We herein speculate that the observed ripples were instabilities associated with the breaking or dissipation of the QMGW (e.g., Carvalho et al., 2017; Hecht et al.,

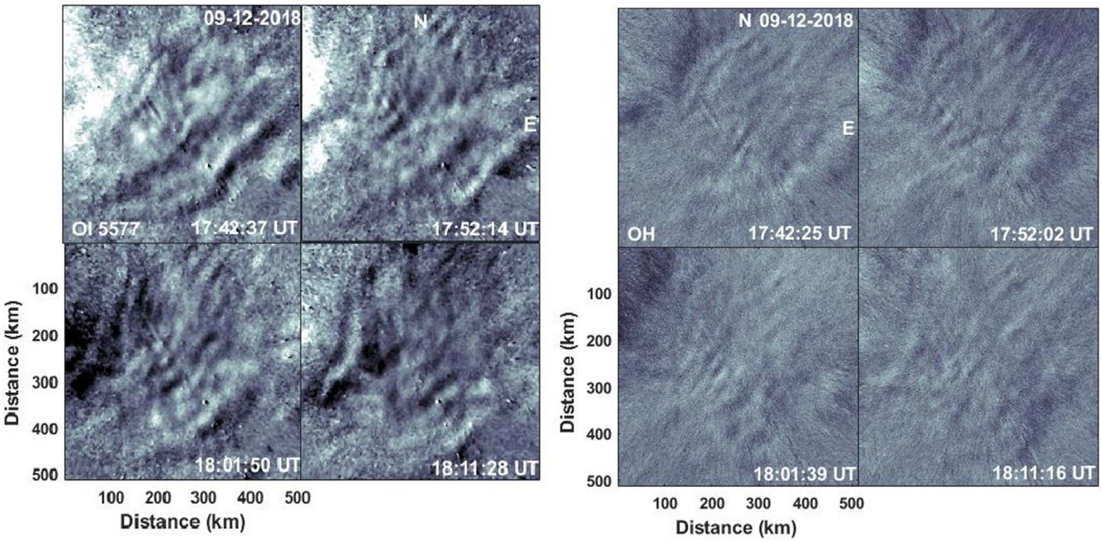

Fig. 3. The wave crest of QMGW breaking into smaller-scale waves is evident in OI 557.7 nm (left panel) and OH (right panel) emission images.

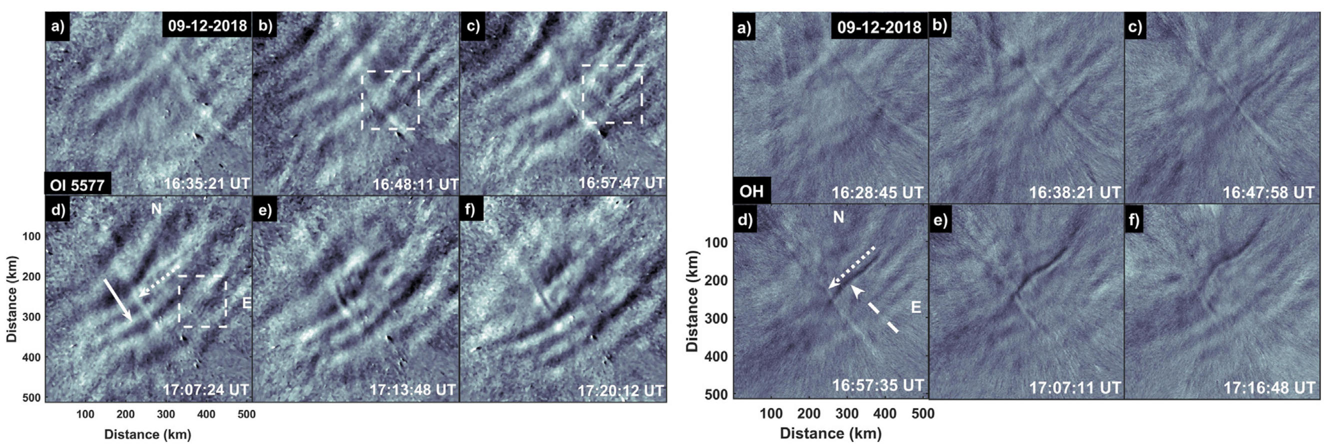

Fig. 4. Images (OI 557.7 nm on the left panel and OH emission on the right panel) projected onto a geographic grid of 512 km × 512 km at their respective emission altitudes. The solid and dashed arrows indicate the direction of propagation of QMGW and front F2 respectively. The dotted arrow indicates the direction of propagation of front F1. A ripple patch observed in OI 557.7 nm emission is highlighted with a rectangular region and can be seen in images (b) to (d) on the left panel.

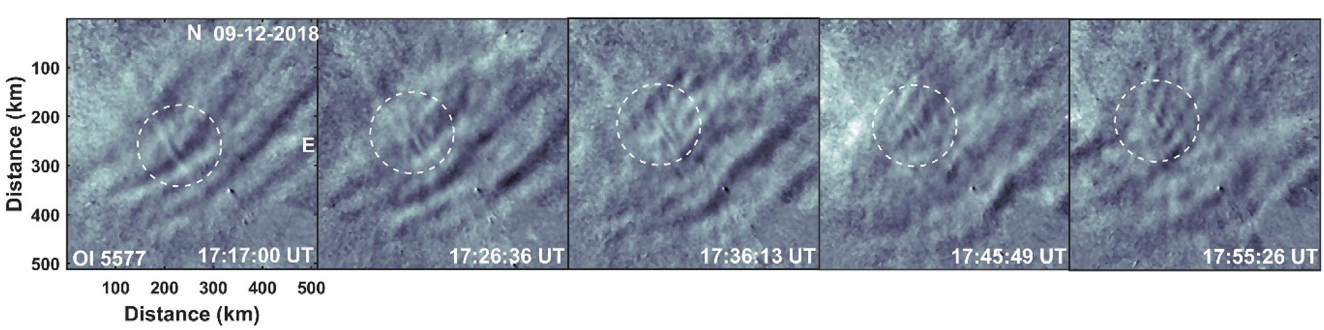

Fig. 5. Selected images of OI 557.7 nm emission showing the fading of wave front of F1 marked by the dotted circle.

2001, 2005; Li et al., 2005; Yamada et al., 2001) or due to the decay of the bore.

Besides the presence of the QMGW and the front F1, another dynamical feature marked by a dark front was observed, but only in the OH emission (marked by the dashed arrow in Fig. 4). This front, hereafter referred to as F2, entered the field of view at 16:22 UT from the south-east sky. The front, aligned in the northeast-southwest direction, propagated towards the northwest at an azimuth of ~315°, which was orthogonal to the propagation

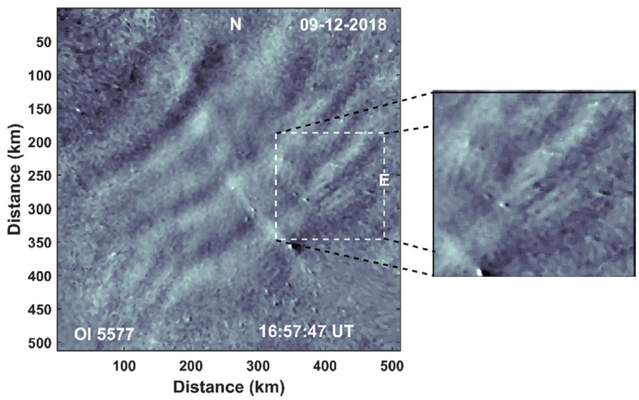

Fig. 6. The OI 557.7 nm emission image showing the ripple structure aligned parallel to background QMGW fronts.

direction of F1 and antiparallel to the propagation direction of QMGW. Undulations were observed behind F2, as the latter crossed the zenith. The occurrence of QMGW at the same time made it difficult to estimate the horizontal wavelength of the undulations. The estimated phase speed of F2 was 63.6 ± 5 m/s, which was nearly double the speed of F1. The front F2 began to fade at 17:48 UT and disappeared from the field of view at 17:58 UT. Though no appreciable change in the direction of propagation was seen, the front revealed a curved shape (undulating front) as it progressed northwest. Such a curvature might arise due to the non-uniform speed of a front along its length (Hozumi et al., 2018). This was in contrast to the front F1 that retained its near straightened shape throughout its propagation across the sky. Both F1 and F2 crossed the zenith simultaneously at ~17:00 UT. As the front F2 was observed only in OH images, any search for complementarity effect did not arise. It was possible that the front was propagating below the peak OH emission altitude (~87 km). As we were not certain about the favourable ducting condition, we refer to F2 as a frontal structure rather than a mesospheric bore.

2.3. Observations on 11 December 2018

On the night of 11 December 2018, the observations carried out until 18:33 UT were obscured by cloud cover, but later the sky became clear. On this night, three filters (OH broadband, OI 557.7 nm and OI 630.0 nm) were used for the observations. The OI 630.0 nm images did not show any wave or ionospheric activity. At 18:51 UT, a dark front (hereafter, F3) entered the field of view of the imager from the northwest part of the sky, as can be seen in the OH images on the right in Fig. 7. The front, observed only in OH emission, propagated at an azimuth of ~140°, i.e., towards the southeast. The observed phase speed of F3 was 34.5 ± 6 m/s. Fig. 7 shows a sample sequence of the processed images of OI 557.7 nm (left panel) and OH (right panel) emissions on 11 December 2018. Since the front F3 was observed only in OH emission layer, we expect a possible ducting structure below the height of the peak OH emission, i.e., 87 km.

3. Discussion

To investigate the background environment during the propagation of QMGW and fronts, we used OH volume emission rate (VER) and temperature profiles retrieved from SABER instrument data sets from the TIMED mission, as mentioned earlier. Dewan and Picard (2001) suggested that a mesospheric bore would require either a thermal or a Doppler duct, or both to propagate. As temperature inversion layers tend to be long-lived phenomena (Meriwether and Gardner, 2000; Meriwether and Gerrard, 2004), it is reasonable to assume that such a layer was present even after the passage of the bore or front. On the night of 9 December 2018, SABER measurements were available ~2 h after the passage of the two fronts (F1/F2) observed, as mentioned earlier (refer Fig. 1 for the locations and times of SABER observations). The squared buoyancy frequency or the Brunt-Väisälä frequency (N^2)

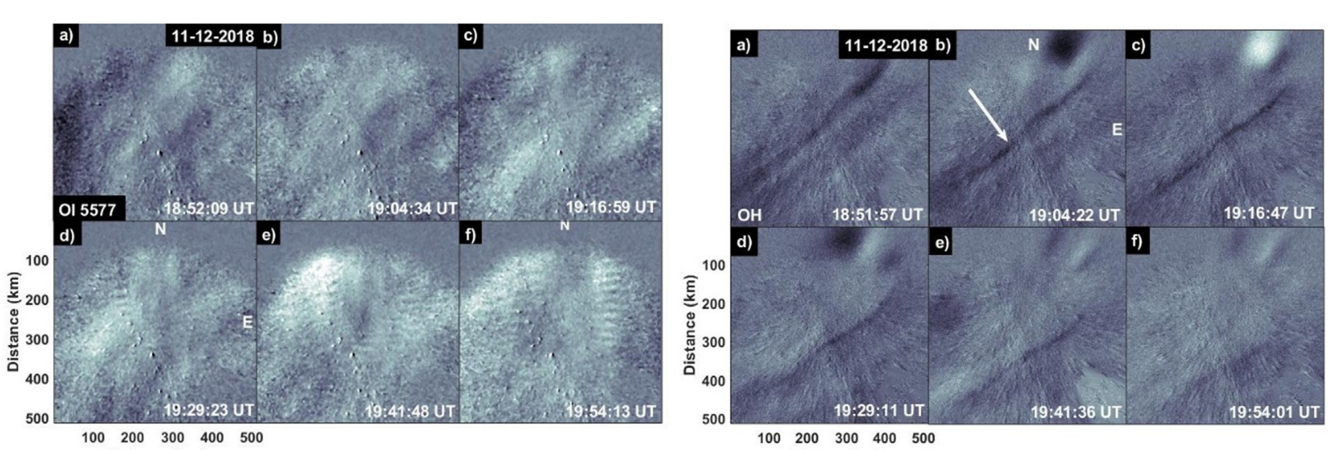

Fig. 7. Selected images of 557.7 nm (left) and OH (right) images obtained on 11 December 2018, projected onto the geographic grid. Solid white arrow in the right panel indicates the propagation direction of front F3.

and the squared vertical wavenumber (m^2) can be obtained from the SABER temperature and HWM14 winds using the following equations (Nappo, 2012):

$$N^2 = \frac{g}{T}\left(\frac{dT}{dZ} + \frac{g}{c_p}\right) \tag{1}$$

where t is temperature, g, the acceleration due to gravity to be taken as 9.53 m/s^2 at the emission altitude and the specific heat c_p being1005 J/Kg/K, and

$$m^2 = \frac{N^2}{(c - U_0)^2} + \frac{U_0''}{c - U_0} - k_h^2 - \frac{1}{H^2} \tag{2}$$

where c is the observed horizontal phase speed of the front, U_0 is the horizontal wind along the front propagation direction, the second derivative of U_o being $U_0'' = d^2U_0/dz^2$, k_h is the horizontal wavenumber and H is the scale height (Isler et al., 1997). Equations (1) and (2) are used to identify the presence of the ducting region, be it thermal (positive N^2 with negative N^2 above and below) or Doppler (positive m^2 with negative m^2 above and below) or both. The SABER temperature and OH VER profiles corresponding to 19:05:26 UT (25.45 °N, 99.18 °E) were the closest to the observation site (refer Fig. 1) and hence they are used in the calculation of N^2 and m^2. In Fig. 8, we show these parameters.

A large temperature inversion, herein referred to as mesospheric inversion layer (MIL), of about ~40 K in the altitude range of 89–95 km can be observed in Fig. 8 (a). Such inversion layers can act as thermal ducts and provide a path for waves or fronts to propagate over large distances, as they have horizontal extension of several hundred km and are long-lived structures (She et al., 2004; Smith et al., 2003; Meriwether and Gerrard, 2004). Owing to the temperature inversion, the N^2 profile shows a region of high stability with positive values surrounded by low stability with low or negative values over the region of 88–97 km. It was likely that this inversion layer was responsible for the propagation of front F1. The squared vertical wavenumber (m^2) shows the presence of a duct layer between 88 and 97 km altitude region (Fig. 8(d)). To assess the nature of the duct, we calculated the contribution of each term in equation (2) (shown in Fig. 8(e)). The first term ($N^2/(c - U_0)^2$) was found to have the largest contribution, followed by the second term ($U_0''/c - U_0$) and much smaller contributions come from the square of the horizontal wavenumber term (k_h^2) and the scale height term ($1/4H^2$). Though it is tempting to conclude that the wind did not have any role to play in forming the duct, these calculations are to be treated with caution, considering that the model winds are known to reveal less shears and therefore could be different from the actual winds. In this context, it may be noted that even without the wind in equation (2), the duct-like structure between heights 88 and 97 km could be seen in the m^2 profile computed for this event.

We have used Dewan and Picard (1998) model to obtain the bore parameters for the front F1. Based on the hydraulic jump theory applicable for a river bore, this model allows calculating the bore parameters such as horizontal wavelength (λ_h), phase speed (c'), amplitude (a), and bore strength (β). The width of the duct after the bore propagation (h_1) is taken as 4.5 km (refer Fig. 8(c)). Following Dewan and Picard (1998), we calculate the undisturbed width (h_0), which turns out to be 3.23 km. Utilising h_0 and h_1, we calculate the bore strength (β) to be 0.39. If $\beta < 0.3$, the energy is dissipated by the generation of waves

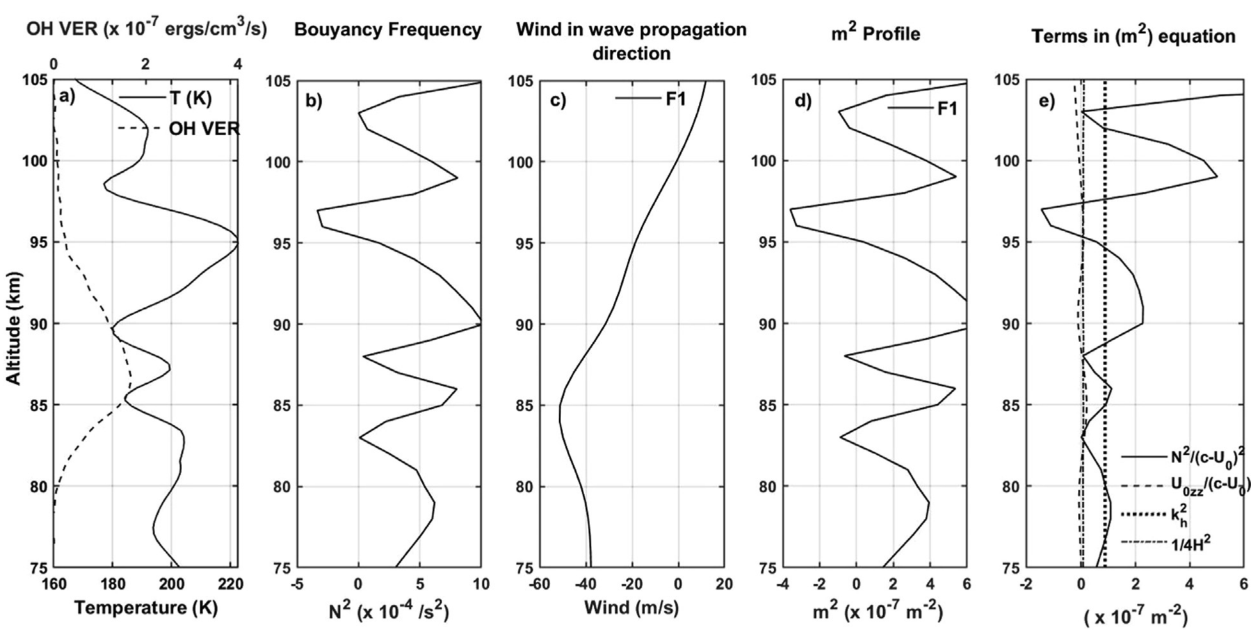

Fig. 8. (a) Temperature (solid line) and OH 1.6 μm VER (dashed line), (b) square of buoyancy frequency, (c) wind in the direction of propagation of front F1 and (d) square of vertical wavenumber, (e) contribution of terms in m^2 equation obtained from SABER and HWM14 model on 9 December 2018.

behind the bore front. Such a feature, wherein the waves are phase-locked to the front, belongs to the category of undular bores. For $\beta > 0.3$ situation, the waves are expected to break and the bore front to propagate with a trailing region of turbulence. This disturbance is referred to as a turbulent (foaming) bore. The model estimated phase speed of the bore was found to be 46.4 m/s, whereas the observed phase speed was 35.6 m/s. The projected wind speed, $U_0 = c - c'$, should then be -10.8 m/s. The horizontal wind from HWM14 wind (see Fig. 8(c)) was 12.1 m/s, which is consistent with the model prediction that the bore must be propagating against the background wind. The bore amplitude (a) from the Dewan and Pickard model turns out to be 1.01 m. The bore parameters are summarised in Table 1. The model predicted and observed parameters are in reasonable agreement, and this supports our inference that the front F1 was a mesospheric bore.

On the night of 11 December 2018, SABER made simultaneous tangent-point measurements of the frontal event, approximately 450 km from the observation site, when the front (F3) was still in the FOV of the imager as shown in Fig. 9(c). The SABER footprint overtook front F3 very close to the observing site on this night. For our analysis, we considered four SABER profiles corresponding to the geographic coordinates (27.92°N, 85.51°E) at 19:28:54 UT, (23.63°N, 88.16°E) at 19:30:22 UT, (20.19°N, 89.96°E) at 19:31:31 UT and (17.95°N, 91.02°E) at 19:32:15 UT labelled as L1, L2, L3 and L4, respectively.

It may be noted that at the time of the SABER pass the location L1 (27.92°N) was behind the front, location L2 (23.63°N) was close to the bore, and locations L3 and L4 (20.19°N and 17.95°N) were ahead of the front. A weak temperature inversion layer of 10–12 K at an altitude of 77–80 km can be seen in Fig. 9(a). It is interesting to note the changes in the OH 1.6 μm peak volume emission rate along the SABER pass in Fig. 9(b). It is well known that the vertical profile of the OH volume emission rate profile inherits a Gaussian-like structure, with a peak at an altitude of 86–87 km in the mesosphere. Some earlier reports even presented a double-peak structure of the volume emission rate (VER) (Melo et al., 2000; Narayanan et al., 2009b). In our case, the location L1 shows the development of a secondary peak at ∼87 km besides the primary peak at 85 km. The subsequent OH emission profile at location L2 shows no distinct peak, and the emission rate was considerably lower, as can also be seen in Fig. 9(b). It was likely that the propagation of the front F3 caused considerable reduction in the OH emission rate. Just ahead of the front and at location L3 (refer Fig. 9(c)), the VER shows two prominent peaks at 80 and 87 km. Further ahead at location L4, the peak at 80 km shows recovery in the emission rate. This observation indicates the possibility that the OH emission rate was significantly modified by the passage of the mesospheric front.

An important question to be addressed is by what mechanism such frontal structures are driven and what could be

Table 1
The observed (values in bracket) and model derived bore parameters.

Parameters of Bore	h_0/h_1 (km)	β	λ_h (km)	U (m/s)	a (km)
9 Dec. 2018	3.23/4.5	0.39	21.25 (*21.2)	46.4 (*35.6)	1.01

* The numbers in the bracket indicate the observed values.

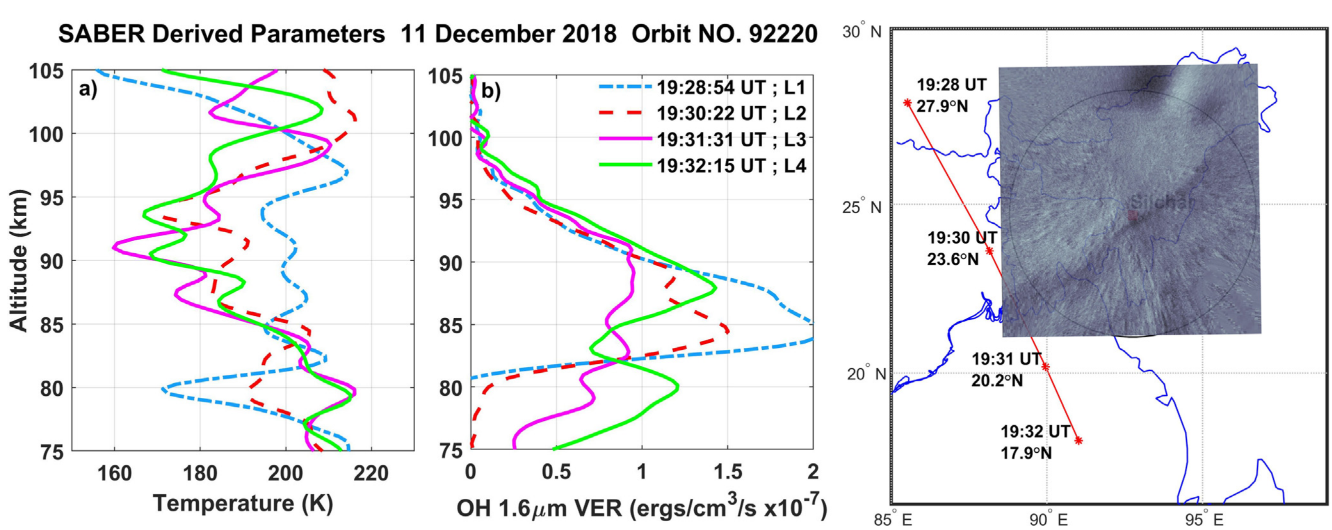

Fig. 9. Profiles of (a) temperature and (b) OH 1.6 μm emission rate obtained from SABER on 11 December 2018. (c) The unwrapped image of front F3 overlaid on map with SABER footprints.

the possible sources. In some previous studies, the fronts were seen to show a curvature and those studies could identify their source location(s) by assuming a radial propagation for the disturbance (like in the case of a tropospheric point-like source) (Smith et al., 2017). In our study, the frontal structure (F1 and F3) observed on 9 and 11 December 2018 and the QMGW observed on 9 December 2018 did not show any curvature (except that F2 showed a curvy structure). This suggests their sources might have been far away (say, greater than 1000 km) rather than being local or close to the observation site. Considering that the propagation of the front F2 was antiparallel to that of the QMGW, we expect there were two different source regions present. The Himalayan mountain range can act as a potential source for orographically generated gravity waves (Liu et al., 2019; Miller et al., 2015; Ramkumar et al., 2021). Furthermore, the Bay of Bengal and the Indian Ocean are known to give rise to convective activity (Bindu et al., 2016; Dutta et al., 2009; Niranjan Kumar and Ramkumar, 2008; Rakshit et al., 2018), when warmer conditions prevail over these large water bodies.

4. Summary

In this work, we present the all-sky imaging observations of two orthogonally propagating frontal systems on 9 December 2018 and another frontal system on 11 December 2018 over Silchar. One among the two frontal events observed on 9 December 2018 displayed the complementarity effect, and it was inferred that this was likely to be a mesospheric bore. The other two frontal events do not show complementarity between the two airglow emissions nor was a duct-like feature observed in N^2 profiles, providing reasons for why they could not be identified as mesospheric bore or wall events. The observations of temperature and OH intensity from the SABER instrument were available for the 9 December 2018 two hours later. We also utilised the horizontal wind measurements from HWM14 in the analysis of the frontal/bore events. It was found the bore propagation was supported by the thermal duct, as inferred from the temperature and N^2/m^2 profiles. Moreover, the parameters obtained from the observed images and those derived from Dewan and Picard (1998) model were in good agreement. As for the night of 11 December 2018, simultaneous SABER observations were available. The analysis for this night brought out the environmental conditions ahead and behind the bore front. A notable finding has been a significant reduction in the OH emission gleaned from SABER observations at the time of the frontal propagation noticed in all-sky images.

A quasi-monochromatic gravity wave was also observed on the night of 9 December 2018 propagating opposite to the direction of propagation of one of the fronts, while at the same time its direction of propagation was orthogonal to that of the other front. During the propagation of bore and QMGW, we also observed ripples in the OI 557.7 nm emission. The phase front of ripples were parallel to the phase front of QMGW and appeared propagating towards the northeast. It is an indication of the operation of dynamical instability on wave propagation, which might have been responsible for the dissipation of QMGW and the appearance of ripples. As more observations from this important site of Silchar are being gathered, our future work is expected to shed light on the contribution of Himalayan orography to the dynamics of this region.

Declaration of Competing Interest

The authors declare that they have no known competing financial interests or personal relationships that could have appeared to influence the work reported in this paper.

Acknowledgements

The authors gratefully acknowledge the SABER team and TIMED mission team for providing useful temperature, OH 1.6 μm VER and pressure data sets. The SABER data can be downloaded from http://saber.gats-inc.com/data.php. One of the authors (N.C.) thanks the Director, Indian Institute of Geomagnetism, for a research fellowship. This work is supported by the Department of Science and Technology, Government of India.

Appendix A. Supplementary material

Supplementary data to this article can be found online at https://doi.org/10.1016/j.asr.2022.05.011.

References

Bageston, J.V., Wrasse, C.M., Batista, P.P., Hibbins, R.E., Fritts, D.C., Gobbi, D., Andrioli, V.F., 2011. Observation of a mesospheric front in a thermal-doppler duct over King George Island, Antarctica. Atmos. Chem. Phys. 11 (23), 12137–12147. https://doi.org/10.5194/acp-11-12137-2011.

Batista, P.P., Clemesha, B.R., Simonich, D.M., Taylor, M.J., Takahashi, H., Gobbi, D., Batista, I.S., Buriti, R.A., De Medeiros, A.F., 2002. Simultaneous lidar observation of a sporadic sodium layer, a "wall" event in the OH and OI5577 airglow images and the meteor winds. J. Atmos. Sol. Terr. Phys. 64.

Bindu, H., Venkat Ratnam, M., Yesubabu, V., Narayana Rao, T., Kesarkar, A., Naidu, C.V., 2016. Characteristics of cyclone generated gravity waves observed using assimilated WRF model simulations over Bay of Bengal. Atmos. Res. 180, 178–188. https://doi.org/10.1016/j.atmosres.2016.05.021.

Brown, L.B., Gerrard, A.J., Meriwether, J.W., Makela, J.J., 2004. All-sky imaging observations of mesospheric fronts in OI 557.7 nm and broadband OH airglow emissions: Analysis of frontal structure, atmospheric background conditions, and potential sourcing mechanisms. J. Geophys. Res. 109, D19104. https://doi.org/10.1029/2003JD004223.

Carvalho, A.J.A., Paulino, I., Medeiros, A.F., Lima, L.M., Buriti, R.A., Paulino, A.R., Wrasse, C.M., Takahashi, H., 2017. Case study of convective instability observed in airglow images over the Northeast of Brazil. J. Atmos. Solar-Terrestrial Phys. 154 (December 2016), 33–42. https://doi.org/10.1016/j.jastp.2016.12.003.

Dewan, E.M., Picard, R.H., 1998. Mesospheric bores. J. Geophys. Res. 103, 6295–6305. https://doi.org/10.1029/97JD02498.

Dewan, E.M., Picard, R.H., 2001. On the origin of mesospheric bores. J. Geophys. Res. 106, 6295–6305. https://doi.org/10.1029/2000JD900697.

Drob, D.P., Emmert, J.T., Meriwether, J.W., Makela, J.J., Doornbos, E., Conde, M., Hernandez, G., Noto, J., Zawdie, K.A., McDonald, S.E., Huba, J.D., Klenzing, J.H., 2015. An update to the Horizontal Wind Model (HWM): The quiet time thermosphere. Earth Space Sci. 2 (7), 301–319. https://doi.org/10.1002/2014EA000089.

Dutta, G., Ajay Kumar, M.C., Vinay Kumar, P., Venkat Ratnam, M., Chandrashekar, M., Shibagaki, Y., Salauddin, M., Basha, H.A., 2009. Characteristics of high-frequency gravity waves generated by tropical deep convection: Case studies. J. Geophys. Res. Atmos. 114 (18), 1–15. https://doi.org/10.1029/2008JD011332.

Fechine, J., Medeiros, A.F., Buriti, R.A., Takahashi, H., Gobbi, D., 2005. Mesospheric bore events in the equatorial middle atmosphere. J. Atmos. Sol. Terr. Phys. 67 (17–18 SPEC. ISS.), 1774–1778. https://doi.org/10.1016/j.jastp.2005.04.006.

Fechine, J., Wrasse, C.M., Takahashi, H., Medeiros, A.F., Batista, P.P., Clemesha, B.R., et al., 2009. First observation of an undular mesospheric bore in a Doppler duct. Annales de Geophysique 27 (4), 1399–1406. https://doi.org/10.5194/angeo-27-1399-2009.

Fritts, D.C., Kaifler, N., Kaifler, B., Geach, C., Kjellstrand, C.B., Williams, B.P., Eckermann, S.D., Miller, A.D., Rapp, M., Jones, G., Limon, M., Reimuller, J., Wang, L., 2020. Mesospheric Bore Evolution and Instability Dynamics Observed in PMC Turbo Imaging and Rayleigh Lidar Profiling Over Northeastern Canada on 13 July 2018. J. Geophys. Res.: Atmos. 125 (14). https://doi.org/10.1029/2019JD032037.

Garcia, F.J., Taylor, M.J., Kelley, M.C., 1997. Two-dimensional spectral analysis of mesospheric airglow image data. Appl. Opt. 36 (29), 7374. https://doi.org/10.1364/ao.36.007374.

Hecht, J.H., Walterscheid, R.L., Vincent, R.A., 2001. Airglow observations of dynamical (wind shear-induced) instabilities over Adelaide, Australia, associated with atmospheric gravity waves. J. Geophys. Res.: Atmos. 106, 28189–28197. https://doi.org/10.1029/2001JD000419.

Hecht, J.H., Liu, A.Z., Walterscheid, R.L., Rudy, R.J., 2005. Maui Mesosphere and Lower Thermosphere (Maui MALT) observations of the evolution of Kelvin-Helmholtz billows formed near 86 km altitude. J. Geophys. Res. 110, D09S10. https://doi.org/10.1029/2003JD003908.

Hozumi, Y., Saito, A., Sakanoi, T., Yamazaki, A., Hosokawa, K., 2018. Undulating wave front of mesospheric bore; Space-borne observations by ISS-IMAP/VISI. Atmos. Chem. Phys. Discuss., 1–10 https://doi.org/10.5194/acp-2018-383.

Isler, J.R., Taylor, M.J., Fritts, D.C., 1997. Observational evidence of wave ducting and evanescence in the mesosphere. J. Geophys. Res. 102, 26301–26313.

Li, F., Liu, A.Z., Swenson, G.R., Hecht, J.H., Robinson, W.A., 2005. Observations of gravity wave breakdown into ripples associated with dynamical instabilities. J. Geophys. Res. D: Atmos. 110 (9), 1–12. https://doi.org/10.1029/2004JD004849.

Li, F., Swenson, G.R., Liu, A.Z., Taylor, M., Zhao, Y., 2007. Investigation of a "wall" wave event. J. Geophys. Res. Atmos. 112 (4). https://doi.org/10.1029/2006JD007213.

Liu, X., Xu, J., Yue, J., Vadas, S.L., Becker, E., 2019. Orographic Primary and Secondary Gravity Waves in the Middle Atmosphere From 16-Year SABER Observations. Geophys. Res. Lett. 46 (8), 4512–4522. https://doi.org/10.1029/2019GL082256.

Medeiros, A.F., Fechine, J., Buriti, R.A., Takahashi, H., Wrasse, C.M., Gobbi, D., 2005. Response of OH, O 2 and OI5577 airglow emissions to the mesospheric bore in the equatorial region of Brazil. Adv. Space Res. 35 (11), 1971–1975. https://doi.org/10.1016/j.asr.2005.03.075.

Medeiros, A.F., Paulino, I., Taylor, M.J., Fechine, J., Takahashi, H., Buriti, R.A., et al., 2016. Twin mesospheric bores observed over Brazilian equatorial region. Ann. Geophys. 34, 91–96. https://doi.org/10.5194/angeo-34-91-2016.

Melo, S.M., Lowe, R.P., Russell, J.P., 2000. Double-peaked hydroxyl airglow profiles observed from WINDII/UARS. J. Geophys. Res. 105 (D10), 12397–12403. https://doi.org/10.1029/1999JD901169.

Meriwether, J.W., Gao, X., Wickwar, V.B., Wilkerson, T., Beissner, K., Collins, S., Hagan, M.E., 1998. Observed coupling of the mesosphere inversion layer to the thermal tidal structure. Geophys. Res. Lett. 25 (9), 1479–1482. https://doi.org/10.1029/98GL00756.

Meriwether, J.W., Gardner, C.S., 2000. A review of the mesosphere inversion layer phenomenon. J. Geophys. Res. Atmos. 105 (D10), 12405–12416. https://doi.org/10.1029/2000JD900163.

Meriwether, J.W., Gerrard, A.J., 2004. Mesosphere inversion layers and stratosphere temperature enhancements. Rev. Geophys. 42 (3), 1–31. https://doi.org/10.1029/2003RG000133.

Miller, S.D., Strak, W.C., Yue, J., Smith, S.M., Joan Alexander, M., Hoffmann, L., Partain, P.T., 2015. Upper atmospheric gravity wave details revealed in nightglow satellite imagery. PNAS 112 (49), E6728–E6735. https://doi.org/10.1073/pnas.1508084112.

Nappo, C.J., 2012. An Introduction to Atmospheric Gravity Waves, 2nd ed. 102, 24–35, Acad. Press

Narayanan, V.L., Gurubaran, S., Emperumal, K., 2009a. Imaging observations of upper mesospheric nightglow emissions from Tirunelveli (8.7°N). Indian J. Radio Space Phys. 38 (3), 50–158.

Narayanan, V.L., Gurubaran, S., Emperumal, K., 2009b. A case study of a mesospheric bore event observed with an all-sky airglow imager at Tirunelveli (8.7°N). J. Geophys. Res. 114, D08114. https://doi.org/10.1029/2008JD010602.

Narayanan, V.L., Gurubaran, S., Emperumal, K., 2012. Nightglow imaging of different types of events, including a mesospheric bore observed on the night of February 15, 2007 from Tirunelveli (8.7°N),. Journal of Atmospheric and Solar-Terrestrial Physics (78–79), 70–83. https://doi.org/10.1016/j.jastp.2011.07.006.

Narayanan, V.L., Nozawa, S., Oyama, S.I., Mann, I., Shiokawa, K., Otsuka, Y., Saito, N., Wada, S., Kawahara, T.D., Takahashi, T., 2021. Formation of an additional density peak in the bottom side of the sodium layer associated with the passage of multiple mesospheric frontal systems. Atmos. Chem. Phys. 21 (4), 2343–2361. https://doi.org/10.5194/acp-21-2343-2021.

Niranjan Kumar, K., Ramkumar, T.K., 2008. Characteristics of inertia-gravity waves over Gadanki during the passage of a deep depression over the Bay of Bengal. Geophys. Res. Lett. 35 (13), 1–5. https://doi.org/10.1029/2008GL033937.

Pautet, P.D., Taylor, M.J., Snively, J.B., Solorio, C., 2018. Unexpected Occurrence of Mesospheric Frontal Gravity Wave Events Over South Pole (90°S). Journal of Geophysical Research: Atmospheres 123 (1), 160–173. https://doi.org/10.1002/2017JD027046.

Rakshit, G., Jana, S., Maitra, A., 2018. Gravity Wave Behavior in Lower Stratosphere during Tropical Cyclones over the Bay of Bengal. Radio Sci. 53 (11), 1356–1367. https://doi.org/10.1029/2018RS006614.

Ramkumar, T.K., Malik, M.A., Ganaie, B.A., Bhat, A.H., 2021. Airglow-imager based observation of possible influences of subtropical mesospheric gravity waves on F-region ionosphere over Jammu & Kashmir, India. Sci. Rep. 11 (1), 1–17. https://doi.org/10.1038/s41598-021-89694-3.

Russell III, James M., Martin G. Mlynczak, Larry L. Gordley, Joseph J. Tansock Jr., and Roy W. Esplin, Overview of the SABER experiment and preliminary calibration results, Proc. SPIE 3756, 277-288. https://doi.org/10.1117/12.366382.

She, C.Y., Li, T., Williams, B.P., Yuan, T., Picard, R.H., 2004. Concurrent OH imager and sodium temperature observations of a mesopause undular bore event over Fort Collins/Platteville, CO. J. Geophys. Res. 109, D22107. https://doi.org/10.1029/2004JD004742.

Smith, S.M., Friedman, J., Raizada, S., Tepley, C., Baumgardner, J., Mendillo, M., 2005. Evidence of mesospheric bore formation from a breaking gravity wave event: Simultaneous imaging and lidar measurements. J. Atmos. Solar – Terrestrial Phys. 67, 345–356. https://doi.org/10.1016/j.jastp.2004.11.008.

Smith, S.M., Stober, G., Jacobi, C., Chau, J.L., Gerding, M., Baumgardner, J.L., et al., 2017. Characterization of a double mesospheric bore over Europe. J. Geophys. Res. 122, 9738–9750. https://doi.org/10.1002/2017JA024225.

Smith, S.M., Taylor, M.J., Swenson, G.R., She, C.-Y., Hocking, W., Baumgardner, J., Mendillo, M., 2003. A multidiagnostic investigation of the mesospheric bore phenomenon. J. Geophys. Res. 108 (A2), 1083. https://doi.org/10.1029/2002JA009500.

Swenson, G.R., Espy, P.J., 1995. Observations of 2-dimensional airglow structure and Na density from the ALOHA, October 9, 1993 'storm flight'. Geophys. Res. Lett. 22 (20), 2845–2848. https://doi.org/10.1029/95GL02795.

Swenson, G.R., Mende, S.B., 1994. Atmospheric airglow imaging with CCDs. Opt. Spectrosc. Tech. Instrum. Atmos. Space Res. 2266, 109. https://doi.org/10.1117/12.187547.

Taylor, M.J., Turnbull, D.N., Lowe, R.P., 1995. Spectrometric and imaging measurements of a spectacular gravity wave event observed during the ALOHA-93 campaign. Geophys. Res. Lett. 22, 2849–2852. https://doi.org/10.1029/95GL02948.

Yamada, Y., Fukunishi, H., Nakamura, T., Tsuda, T., 2001. Breaking of small-scale gravity wave and transition to turbulence observed in OH airglow. Geophys. Res. Lett. 28 (11), 2153–2156. https://doi.org/10.1029/2000GL011945.